A Conformable Force/Tactile Skin for Physical Human–Robot Interaction

A. Cirillo, F. Ficuciello, C. Natale, S. Pirozzi, and L. Villani

***Abstract*—In this letter, a new sensorized flexible skin has been used to enhance safety and intuitiveness of physical human–robot interaction (HRI) in applications where both intentional and unintentional contacts may occur. The new technological contribution with respect to other skin sensors consists of the capability of measuring both the position of the contact point and the three components of the applied force with high repeatability and accuracy. To show how this innovative technology enables the exploitation of control laws for intuitive HRI, two standard control strategies have been implemented to perform both manual guidance with multiple contact points and safe reaction in case of unintentional collision detection, at the same time. In both cases, an admittance control scheme with a second order kinematic control is adopted. A multi-priority redundancy resolution strategy is implemented in the case of manual guidance. The experimental verification of the sensor capabilities is made using a patch of the skin installed on a link of a KUKA LWR4 robot.**

***Index Terms*—Force and Tactile Sensing; Physical Human-Robot Interaction.**

I. Introduction

A big challenge in robotics research is the developments of robotics systems, like humanoids, flying robots, assistant and medical robots, with a high level of autonomy, able to cooperate and interact each other as well as with humans. Autonomous or cooperative tasks require that the robots should operate without producing damages to themselves, to humans and to other surrounding objects. Sensing becomes fundamental, and tactile sensing is particularly important since many tasks require the robot to recognise unintentional collisions or to make intentional physical contact with objects or humans.

Safe and efficient physical HRI requires the knowledge of interaction forces and contact locations in order to perform cooperation and co-manipulation tasks and to limit damage from accidental impacts. This crucial information can be obtained through direct measurements or by estimation techniques using different methods depending on the available technology.

Manuscript received August 31, 2015; revised November 13, 2015; accepted November 18, 2015. Date of publication December 3, 2015; date of current version January 1, 2016. This paper was recommended for publication by Associate Editor J. McInroy and Editor J. Wen upon evaluation of the reviewers' comments. This work was supported by the EC Seventh Framework Programme within SAPHARI (287513) and RoDyMan (320992) projects.

A. Cirillo, C. Natale, and S. Pirozzi are with the Dipartimento di Ingegneria Industriale e dell'Informazione, Seconda Università degli Studi di Napoli, Aversa 81031, Italy (e-mail: andrea.cirillo@unina2.it; ciro.natale@unina2.it; salvatore.pirozzi@unina2.it).

F. Ficuciello and L. Villani are with the Dipartimento di Ingegneria Elettrica e Tecnologie dell'Informazione, Università degli Studi di Napoli, Napoli 80125, Italy (e-mail: fanny.ficuciello@unina.it; luigi.villani@unina.it).

Digital Object Identifier 10.1109/LRA.2015.2505061

In the last decade, different kinds of artificial skins have been developed. Most of them [1]–[8] are based on tactile sensing and are able to measure the contact point where a force is applied. For example, in [1] the authors presents a tactile skin based on a set of distributed capacitive tactile sensing elements that have been integrated on the iCub cognitive robot covering the limbs and providing a tactile feedback, in terms of contact points, for possible contacts with the environment. Information such as force magnitude and direction is not easily reconstructed. In fact, as reported in [9]–[11], the estimation and the control of the interaction forces need for additional sensors installed in the robot limbs, i.e., six axes force/torque sensors, as well as knowledge of the dynamic model of the robot.

The prevailing trend of the research in this field is that to cover the whole body of the robot or some of its parts with an array or patches of tactile/force sensors that use nearly all modes of transduction: resistive, capacitive, ultrasonic, magnetic, piezo-electric. Dahiya et al. [12] provide an exhaustive review on tactile skin technology and on its features highlighting various requirements and expectations such as flexibility/conformability, spatial resolution, wiring problems and technologies for communication and data transmission. It can be recognised that, while the use of tactile sensors in the contact point detection and pressure estimation is a diffuse practice, the development of a distributed sensor able to estimate both the magnitude and the direction of the applied forces is still an open challenge for robotic researchers.

On the other hand, indirect estimation of the interaction forces can be obtained using alternative techniques. One of the most effective approaches proposed in the literature is that based on the residual method, which allows to estimate the joint torques generated by the external forces applied to the body of a robot manipulator [13]. This information, together with the measurement of the contact location, that can be obtained, e.g., with tactile sensing or depth cameras, allows to compute a good estimation of the external force, also in the case of multiple contacts [14]. The residual technique has been successfully employed also by the authors of this letter in applications where force feedback is required to control the intentional physical HRI, as in [15]–[17]. The nice feature of the residual method is that it does not require the installation of force sensors on the robot, although exteroceptive sensing is needed for the identification of the contact locations. A drawback is that, as all the model-based techniques, an accurate knowledge of the robot dynamic model is required; some dynamic parameters, like the robot payload, and some torque disturbances, like the joint friction, are uncertain and may change during robot operation.

Another disadvantage with respect to the skin solution is that the forces and moments that do not produce joint torques (i.e., those that are balanced by the mechanical structure) cannot be measured. Finally, the accuracy of the estimation depends on the location of the contact point on the robot structure.

In this work, the authors present a new skin prototype, developed from the rigid solution described in [18], able to estimate both the contact point(s) and the force vector(s). The new prototype has been also designed so that it can be conformed to the external surface of the robot. A patch of the skin has been produced, conformed, installed on a 7-DOF KUKA LWR4 manipulator and tested with two standard control strategies, based on already published works and chosen to highlight all sensor capabilities. The first one realises the manual guidance using multiple contact points on the robot body for human-robot collaboration; the second one consists of a safe reaction strategy that uses the skin to detect unintentional collisions and properly react to ensure safety. Both strategies are based on admittance control and on the second order kinematic control formulation. A multi-priority redundancy resolution strategy at acceleration level, proposed in [19] by the authors of this letter, is implemented in the case of manual guidance.

II. The New Conformable Skin

A. The Working Principle

The working principle of the sensitive skin has been originally used for the development of a force/tactile sensor [20]. On the basis of that idea the authors of this letter designed the rigid artificial skin detailed in [18], whose working principle is here recalled. It is based on the use of a standard rigid PCB (Printed Circuit Board) constituted by 36 identical *sensing modules*, each capable of measuring the contact force vector that acts on it. In particular, each sensing module is constituted by four *taxels* organised in a 2×2 matrix. Each taxel consists of an optical LED/PT (Light Emitting Diode/PhotoTransistor) couple spectrally matched. A deformable silicone cap is positioned above the 4 optoelectronic couples for each sensing module. This cap has a hemispherical shape on the top side, while on the bottom side it presents four empty cells into the material, vertically aligned with the four optoelectronic couples. In the rest condition, a part of the light, emitted by the LEDs and reflected by the four cells, reaches the PTs. When an external force is applied to the deformable layer, it produces deformations for all the four taxels constituting a sensing module. These deformations produce variations of the reflected light and, accordingly, of the photocurrents measured by the PTs. The interested reader may find in [18] all the details concerning the technologies adopted to realise both optoelectronic and deformable layers, the description of the taxel interrogation strategy, the full characterization of the rigid skin prototype and some pictures. In the following of this section only the differences between the new flexible version with respect to the rigid version, deeply detailed in [18], are highlighted.

B. The Design of the Flexible PCB

The new conformable version of the artificial skin is based on the use of the flexible PCB technology to produce the optoelectronic layer, in order to make it conformable to different curved surfaces. This technology is the most convenient solution in terms of flexibility and cost. Concerning the maximum reachable flexibility, some observations are needed. In particular, the installation of the electronic components on the flexible PCB reduces the flexibility property, depending both on the number and the dimensions of the components. Again, also the number of layers necessary for the wiring affects the flexibility. By exploiting some characteristics of the rigid version of the skin, briefly recalled below, the optoelectronic layer has been suitably re-designed in order to maximise the reachable flexibility for the conformable version of the skin.

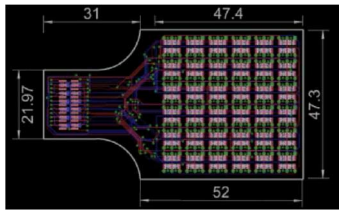

Fig. 1. Sensor patch PCB (the dimensions are expressed in millimeters).

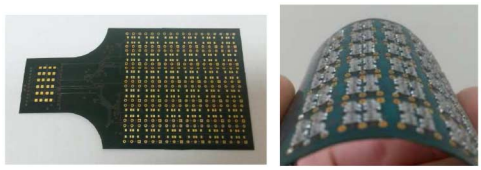

(a) (b)

Fig. 2. Pictures of the realized flexible PCB before (left) and after (right) the optoelectronic components mounting.

The selected optoelectronic components are both manufactured by OSRAM: the LED (code SFH4080) is an infrared emitter with a peak wavelength of 880 nm; the PT is a silicon NPN phototransistor (code SFH3010) with a peak sensitivity at 860 nm wavelength. The conditioning electronics is constituted by simple resistors without amplification and/or filtering stages, since the measured voltages are sufficiently high to be directly converted by using an ADC. As a consequence, the sensing modules are only constituted by optoelectronic components that have SmartLED package 0603, and additional resistors to drive the LEDs with package 0402. Since no additional Integrated Circuits (ICs) with cumbersome package are necessary for the conditioning electronics, the minimum number of components to mount on the flexible PCB, for each taxel, is three. The packages of these components are small enough to maintain an high flexibility for the PCB also after the soldering. Furthermore, the adopted scanning strategy for the sensing modules, detailed in [18], allows a simplification for the wiring, by reducing the number of layers needed, once again helping to improve the PCB flexibility. In particular, to interrogate the 36 sensing modules (corresponding to 144 taxels) of the flexible skin patch designed for this letter, the minimum number of wires is 25: 12 AD channels, 12 digital I/O and the ground. With this choice, the routing of a whole skin can be completed by using a flexible PCB with only 4 layers (Fig. 1). The adopted solution, after soldering all the components, maintains a high flexibility (Fig. 2) that allows the skin patch to be conformable to a surface with

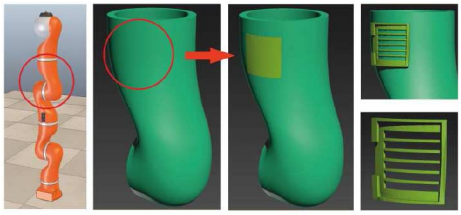

(a) (b) (c) (d)

Fig. 3. Skin support: a) the KUKA LWR4 3D arm model, b) selected surface, c) extruded shape d) designed skin support.

(a) (b) (c)

Fig. 4. Flexible skin prototype during assembly phases: a) perspective view with some silicone caps bonded, b) perspective view with all silicone caps, c) completed skin prototype after the second silicone molding.

minimum curvature radius of 2-3 cm. This curvature is sufficient for any applications that require to cover robot surfaces such as arms, legs, torso. Figure 1 also reports the dimensions of the sensor. The active surface of the skin patch (corresponding to the sensing elements) is about $47 \times 47\,\mathrm{mm}^2$, while the 25 wires, needed to interrogate the patch, are routed to a standard connector positioned on the left side.

C. Integration on the Robot

After completing the assembly of the electronic components on the flexible PCB and before to start the bonding of the silicone caps, the flexible patch has to be conformed to the surface selected for the final assembly of the completed skin. With this objective, a mechanical support, designed on the basis of the surface shape selected for the final mounting of the skin patch, has to be realized. In this work, the flexible skin patch has been realised to be installed on a KUKA LWR4. Given a CAD model of the robotic arm surface, the sensor support has been designed and realized in ABS material with a 3D rapid prototyping printer. The 3D CAD model provides a simple way to extract a patch of the robot surface on which to collocate the distributed sensor. Figure 3 shows how the skin support has been designed starting from the CAD model of the whole arm (a), on which the area identified for the final mounting of the skin patch is highlighted (b). From the selected surface the skin support has been extruded as a filled solid (c). The obtained solid has been finished by obtained the final skin support (d), which shows side edges designed to mechanically block the sensor patch on it and also several holes that allows the inspection of the bottom side of the electronic layer in case of damages. Hence, the flexible PCB, only with the soldered optoelectronic components, has been mounted on the designed support, by acquiring the desired shape conformed to the KUKA LWR4. Finally, silicone caps have been bonded on the conformed flexible PCB. In order to increase the mechanical robustness of the whole sensor, the bonded silicone caps have been connected all together by using a second silicone molding on the basis of the FE analysis presented by the authors in [21]. The selected hardness for the second molding guarantees a negligible coupling between neighboring sensing modules. Figure 4 shows some pictures of the flexible skin prototype during the assembling phases. Note that the final obtained conformed patch, differently from the rigid version, has a non-uniform spatial resolution for the force detection, which depends on the local curvature. Let r_{flat} denote the sensing modules distance before the bonding of the PCB on the conformed mechanical support, that is equal to the spatial resolution of the rigid version, namely, 7.4 mm. Moreover, let R denote the local curvature radius of the mechanical support and h_c the height of the silicone caps. Then, the spatial resolution of the conformed skin locally varies of $\pm(h_c r_{flat}/R)$ from the flat value r_{flat}. In particular, by considering a curvature radius of $R = 30$ mm, being $h_c = 4$ mm and $r_{flat} = 7.4$ mm, the estimated spatial resolution of the flexible skin varies of ± 1 mm from the spatial resolution of the rigid version, by resulting in a non-uniform resolution equal to 7.4 ± 1 mm.

D. Calibration of the Conformed Patch

The assembly of the sensor (e.g., components soldering, bonding of the silicone caps, molding of the low-hardness silicone) could introduce differences in the response of the skin modules. Hence, the calibration approach depends on the specific application. Some robotic applications (e.g., collision detection, advanced robot programming methods, human safety) can require the estimation of contact points and the estimation of the contact force vectors for large areas with a good repeatability and sufficient accuracy. In these cases, as discussed in [18], the same calibration matrix can be used for all the sensing modules of the whole skin patch. In other applications (e.g., human-robot, robot-robot and robot-environment interactions) that require better repeatability and accuracy in the force vector estimation a calibration procedure for each sensing module is advised. For this work, where HRI experiments are presented, the calibration of the skin patch has been made separately for each sensing module. A specific procedure has been implemented for the conformed skin, by taking into account that the prototype has a curvature locally varying, according to the shape of the area selected for the integration. First of all, the skin patch has been mounted, by using a mechanical adapter, on the reference sensor: the six-axis load cell FTD-Nano-17, by ATI. To collect data for the calibration of the skin patch, two experiments for each sensing module have been carried out, by using a stiff plane and by applying different external forces. In particular, an operator manually interacted with each sensing module being careful to apply forces with components along all the axes of the frame of the sensing module, and with amplitudes varying from the value 0 to the sensor full scale. The force components applied to each sensing module are similar to those of the validation example reported in Fig. 6, detailed in the following. For each experiment, all the voltage variations measured by the phototransistors belonging to the sensing module

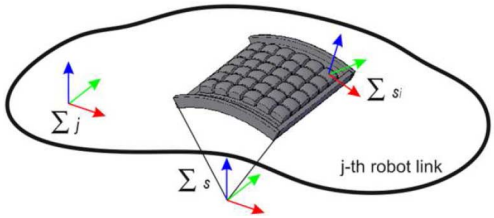

Fig. 5. Definition of sensor frames.

involved in the contact, and the force components measured by the reference load cell, have been acquired. Then, for each experiment, the force vector applied on the i-th sensing module and measured by the reference sensor $\boldsymbol{f}_i^s$ has been expressed in the sensing module frame s_i, taking into account the orientation of each sensing module with respect to the load cell represented by the rotation matrix $\boldsymbol{R}_{s_i}^s$, in order to obtain the force vector expressed in the sensing module frame

$$\boldsymbol{f}_i^{s_i} = \boldsymbol{R}_s^{s_i} \boldsymbol{f}_i^s \qquad i = 1, \ldots, 36. \tag{1}$$

The rotation matrices $\boldsymbol{R}_{s_i}^s$ can be obtained from the CAD model of the skin support described in Sec. II-C, where the sensor frame s and the the sensing module frames s_i have been defined as reported in Fig. 5. Note that the reference sensor has been mounted to the mechanical skin support so as to align its frame with the sensor frame s. Only the use of these re-oriented data guarantees a good calibration, since the phenomenological model, defined in [18], that relate the external force vector (applied to the silicone cap) and the measured voltages (related to the cell deformations), is usable only if the force vector is expressed in the local frame. The collected data, for each sensing module, have been split in two sets: a training set used to identify the calibration parameters and a validation set (not used in the training) used to validate the accuracy of the calibration. The phenomenological model used for the calibration is a linear combination of the voltage variations, corresponding to a 3×4 matrix of calibration parameters for each sensing module. The calibration parameters, identified from the training data with a least square algorithm, have been used to evaluate the accuracy of the calibration phase, by computing the estimated force components for the validation data set. Figure 6 shows the accuracy of the calibration, by reporting, for a sensing module, the estimated and the measured force components using the validation data set. Taking into account that the full scales are 10N for the z component and ± 3 N for the other components, the resulting accuracy is good for all the force components and for all the sensing modules. In fact, the estimation mean error is equal to 0.14N for the x component, 0.10N for the y component and 0.33N for the z component.

III. Control Strategies for Sensor Testing

Two standard control strategies have been implemented, in order to highlight all sensor capabilities. In particular, both the cases of intentional and unintentional contacts have been considered. In the case of intentional contacts, the forces measured by skin are used to manually guide the robot through multiple contact points. In the case of unintentional collisions detected

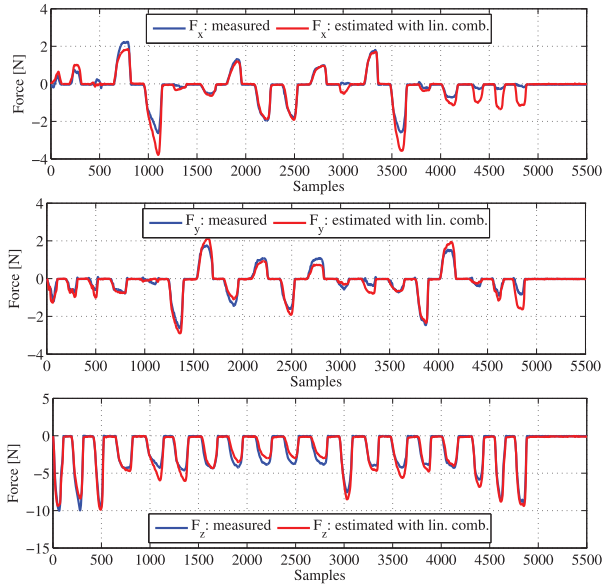

Fig. 6. Force components for a validation data set: x component (top), y component (middle), z component (bottom).

by the skin, the measured forces are used to achieve a safe reaction strategy.

Two contact points are considered: one ($\boldsymbol{p}_e \in \mathbb{R}^3$) is located on the end effector and the other ($\boldsymbol{p}_b \in \mathbb{R}^3$) is located on a link of a 7-DOF robot. Let $\boldsymbol{f}_e \in \mathbb{R}^3$ and $\boldsymbol{f}_b \in \mathbb{R}^3$ be the corresponding contact forces. The robot control law is a standard position control in the joint space, which allows to track a suitable reference joint trajectory $\boldsymbol{q}_r(t) \in \mathbb{R}^7$. This reference trajectory is computed according to a multi-priority algorithm for manual guidance or according to a collision reaction algorithm, depending on the magnitude of the sensed force $\boldsymbol{f}_b$, i.e.,

$$\boldsymbol{q}_r(t) = \begin{cases} manual\ guidance, & \text{if } \|\boldsymbol{f}_b\| \leq f_{th}, \\ collision\ reaction, & \text{if } \|\boldsymbol{f}_b\| > f_{th}, \end{cases} \tag{2}$$

being $f_{th} > 0$ a suitable threshold.

In the case of *manual guidance*, $\boldsymbol{q}_r(t)$ is computed on the basis of suitable dynamic relationships, or admittances, between the sensed contact forces and the displacements of the contact points, as explained below. For a generic contact point $\boldsymbol{p}_c$, with $c = e, b$, the reference acceleration $\ddot{\boldsymbol{p}}_{c,r}$, velocity $\dot{\boldsymbol{p}}_{c,r}$ and position $\boldsymbol{p}_{c,r}$ are computed from the force $\boldsymbol{f}_c$ measured in the contact point by integrating the admittance equation:

$$\ddot{\boldsymbol{p}}_{c,r} = \boldsymbol{M}_c^{-1}(\boldsymbol{f}_c - \boldsymbol{D}_c \dot{\boldsymbol{p}}_{c,r}), \tag{3}$$

where $\boldsymbol{M}_c, \boldsymbol{D}_c \in \mathbb{R}^{3\times 3}$ are suitable positive definite matrix gains, with the meaning of mass and damping respectively. In other words, the quantities $\ddot{\boldsymbol{p}}_{c,r}$, $\dot{\boldsymbol{p}}_{c,r}$, $\boldsymbol{p}_{c,r}$ represent the desired compliant motion of a virtual body located at point $\boldsymbol{p}_c$ with mass $\boldsymbol{M}_c$ and damping $\boldsymbol{D}_c$ under the action of the contact force $\boldsymbol{f}_c$.

Since the two contact points belong to the same kinematic chain, their motion cannot be assigned arbitrarily and conflicting situations may occur. These conflicts can be managed by the control through a suitable task priority strategy. Depending on the specific situation, the motion of one of the two contact points is considered as the main task, while the motion

of the other point is considered as a secondary task. Only the motion components of the secondary task that are not conflicting with the main task, i.e., those projected in the null space of the Jacobian of the main task, will be executed.

The main task can be defined, for example, at the point which is touched first. Therefore, when the human applies a force $\boldsymbol{f}_e$ to the end effector (point $\boldsymbol{p}_e$) first, and then applies a force $\boldsymbol{f}_b$ to the robot's body (at point $\boldsymbol{p}_b$), the latter will cause a reconfiguration of the robot's body that does not affect the motion of $\boldsymbol{p}_e$, which depends only on $\boldsymbol{f}_e$. Vice versa, if the human applies first a force $\boldsymbol{f}_b$ to the robot's body at point $\boldsymbol{p}_b$, then the motion of point $\boldsymbol{p}_b$ will depend only on $\boldsymbol{f}_b$, also in the case that another force will be applied at the end effector.

By adopting the multi-priority control formulation presented [19], the joint space reference acceleration $\ddot{\boldsymbol{q}}_r(t)$ can be computed as

$$\ddot{\boldsymbol{q}}_r = \boldsymbol{J}_e^{\#}(\boldsymbol{r}_e - \dot{\boldsymbol{J}}_e\dot{\boldsymbol{q}}_r) + \bar{\boldsymbol{J}}_b^{\#}(\boldsymbol{r}_b - \dot{\boldsymbol{J}}_b\dot{\boldsymbol{q}}_r - \boldsymbol{J}_b\boldsymbol{J}_e^{\#}(\boldsymbol{r}_e - \dot{\boldsymbol{J}}_e\dot{\boldsymbol{q}}_r)), \tag{4}$$

where $\boldsymbol{J}_e^{\#}$ is the generalised inverse of the end-effector Jacobian $\boldsymbol{J}_e \in \mathbb{R}^{3\times 7}$, $\bar{\boldsymbol{J}}_b^{\#} = (\boldsymbol{I} - \boldsymbol{J}_e^{\#}\boldsymbol{J}_e)\boldsymbol{J}_b^{\#}$ is the generalised inverse of the the contact point Jacobian $\boldsymbol{J}_b \in \mathbb{R}^{3\times 7}$ projected into the null space of $\boldsymbol{J}_e$, while the resolved acceleration vectors $\boldsymbol{r}_c \in \mathbb{R}^3$, with $c = e, b$ are computed as

$$\boldsymbol{r}_c = \ddot{\boldsymbol{p}}_{c,r} + k_d(\dot{\boldsymbol{p}}_{c,r} - \boldsymbol{J}_c\dot{\boldsymbol{q}}_r) + k_p(\boldsymbol{p}_{c,r} - \boldsymbol{k}_c(\boldsymbol{q}_r)), \tag{5}$$

being k_d, k_p strictly positive gains. The reference vectors $\ddot{\boldsymbol{p}}_{c,r}$, $\dot{\boldsymbol{p}}_{c,r}$ and $\boldsymbol{p}_{c,r}$ are computed using the equation (3), while the vector $\boldsymbol{k}_c(\boldsymbol{q}_r)$ is the contact point position computed from $\boldsymbol{q}_r$ using the forward kinematics mappings $\boldsymbol{k}_c(\boldsymbol{q}_r)$, with $c = e, b$.

Equation (4) assumes that the motion of point $\boldsymbol{p}_e$ has higher priority with respect to the motion of point $\boldsymbol{p}_b$. The change of priority can be achieved using the same equation, by replacing the subscript e with the subscript b and viceversa. Notice that, when the Jacobians are close to a singularity, high joint acceleration and speed can be generated yielding high tracking errors and possibly dangerous situations. To mitigate such effects the generalised inverse can be robustly calculated using the damped least squares pseudo-inverse [22]. The same admittance strategy can be also used to manage unexpected collisions, i.e., a *collision reaction* when the threshold f_{th} in (2) is overcome. In this case, a safe reaction is commanded to the robot according to the following criterion. The primary task is interrupted and a motion of the detected contact point is commanded still according to the admittance equation (3), but $\boldsymbol{M}_c$ and $\boldsymbol{D}_c$ are suitably selected so as the reaction time and the magnitude of the repulsive acceleration generate a quick reflex motion of the robot. In particular, the point where the collision is detected by the sensitive skin, moves in the same direction of the applied force. Hence, the reference joint space acceleration becomes

$$\ddot{\boldsymbol{q}}_r = \boldsymbol{J}_c^{\#}(\ddot{\boldsymbol{p}}_{c,r} - \dot{\boldsymbol{J}}_c\dot{\boldsymbol{q}}_r + k_d(\dot{\boldsymbol{p}}_{c,r} - \boldsymbol{J}_c\dot{\boldsymbol{q}}_r) + k_p(\boldsymbol{p}_{c,r} - \boldsymbol{k}_c(\boldsymbol{q}_r))). \tag{6}$$

In turn, the reference joint space trajectory $\boldsymbol{q}_r(t)$ in (2) can be computed by integrating (4) for manual guidance or (6) for collision reaction. Notice that, since the Jacobian J_c has null columns from 4 to 7, the accelerations of the joints from 4 to 7 computed using equation (3) are null. Therefore, the corresponding robot links freeze just after the collision.

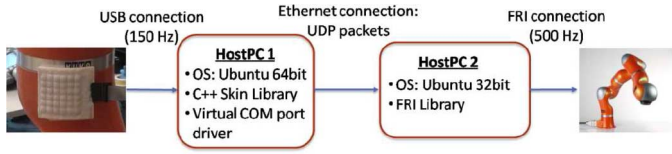

Fig. 7. Experimental setup block diagram.

Fig. 8. The skin sensor installed on the 3rd link of the KUKA LWR4.

IV. Experimental Results

This section aims to show how the sensor can be used to recognize simultaneously intentional and unintentional contacts and how the robot can react in different way exploiting the information on the contact force. The video attached to this letter shows the whole experimental verification.

A scheme of the setup is shown in Fig. 7. A conformable skin patch is installed on the third link of the KUKA LWR4 (Fig. 8) as described in Sec. II-C. With this choice the number of joints from the base to the contact point is enough to move the contact point along any direction of the Cartesian space. The sensor is connected to an acquisition board with a flat cable (Fig. 8). The acquisition board chosen to digitize the sensor voltages is the STM32F3 Discovery board based on a STM32F303 ARM Cortex-M4 microcontroller. It sends over an USB connection the acquired raw data to a HostPC, at a sampling frequency of 150 Hz, on which a C++ Skin Library is running. The latter is able to provide, on the basis of the sensor voltages, the estimated force vectors applied to the 36 skin sensing modules and the contact point(s). The information, then, are sent via an UDP socket to a second PC used to compute the control algorithm. To work properly, the KUKA controller requires that the commanded joint positions values have to be updated with a rate of at least 500 Hz. So, a different thread is used to asynchronously acquire the sensor data. The second host is interfaced with the KUKA LWR4 robot with the KUKA FRI Library.

The force $\boldsymbol{f}_b$ measured with the skin sensor and used in the control (and in particular in (3) written with $c = b$) is defined as the net force acting on the whole contact surface of the skin patch, computed as

$$\boldsymbol{f}_b = \boldsymbol{R}_s \sum_{i=1}^{36} \boldsymbol{f}_i^s, \qquad \boldsymbol{R}_s = \boldsymbol{R}_j \boldsymbol{R}_s^j \tag{7}$$

where $\boldsymbol{f}_i^s$ is the force measured by the $i-$th skin sensing module as defined in Sec. II-D, $\boldsymbol{R}_s^j$ is the rotation matrix

that expresses the orientation of the sensor frame w.r.t. the robot j-th link and $\boldsymbol{R}_j$ is the rotation matrix of j-th link w.r.t. the robot base frame. The control parameters have been selected by choosing in equation (3) the scalar matrices: $\boldsymbol{M}_e = m_e\boldsymbol{I}_3$, $\boldsymbol{D}_e = d_e\boldsymbol{I}_3$, $\boldsymbol{M}_b = m_b\boldsymbol{I}_3$, $\boldsymbol{D}_b = d_b\boldsymbol{I}_3$. With this choice the response times for the end effector and the body control points are proportional to m_e/d_e and m_b/d_b, respectively, while the magnitudes of the repulsive velocities are proportional to $1/d_e$ and $1/d_b$, respectively. In the experiments the following values have been selected: $m_e = 25$ kg, $d_e = 6$ Ns/m, $m_b = 0.5$ kg, $d_b = 2$ Ns/m, $k_p = 50$ s^{-2} and $k_d = 10$ s^{-1}. This choice ensures a well damped response for both contact points with a quicker reaction time for the body control point.

A. *First Experiment*

The objective of the first experiment is to show how the skin can be used to intentionally interact with the robot and to safely react to unintentional contacts at the same time. With this aim, the control law in (2) has been implemented. In particular, the robot is programmed to follow, as primary task, a periodic trajectory at the end effector. Figure 9(a) reports the desired trajectory at the end effector that corresponds to a horizontal line in the space. A threshold equal to 7N has been fixed for the skin. In the first 8 s, the primary task is correctly executed with a trajectory error near to zero (Fig. 9(d)), while no contacts occur with the skin (Fig. 9(b)). During the task execution, an intentional contact is applied to the skin in order to reconfigure the robot in an elbow configuration which is more comfortable for the user that has to act in the robot workspace. The contact occurs between 8 s and 10 s and the detected force, reported in Fig. 9(b), is below the established threshold. Thus, the desired motion in Fig. 9(c), computed at the contact point, is projected in the null space of the first task, which is then preserved, as the low trajectory error demonstrates in Fig. 9(d). Figure 9(e) reports the angles of joints 2, 3 and 4 that move the elbow. Given the initial joints configuration ($q_2 > 0$ and $q_4 < 0$), the robot moves along the prescribed trajectory, in absence of contacts, in the elbow-up configuration (first 8 s). By applying a proper force and by exploiting the redundant DOFs, the user is able to safely move the robot from the elbow-up ($q_3 > -1.57$ rad) to the elbow-down ($q_3 < -1.57$ rad), while the robot still executes the main task (between 8 s and 10 s). Then, at 16 s, a second contact occurs and this time the force exceeds the threshold. Hence, the robot controller interprets the force as an unintended collision, and it imposes to the collision point a motion in the Cartesian direction of the collision force, to preserve the safety of the human. The correctness of the collision reaction can be assessed by comparing Figs. 9(b) and 9(c), which show that the velocity of the contact point is substantially aligned to the force direction. Just after the collision, the primary task is abandoned and when the contact force falls to zero, the robot stops (see last 9 s). Obviously, the robot could be programmed to resume the interrupted operation as soon as the contact is no longer detected. To assess the safety of the reflex motion, besides the direction of the motion that has been already shown coherent with the applied force, the reaction time

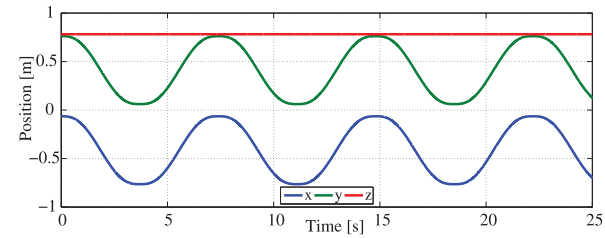

(a) Desired end-effector trajectory.

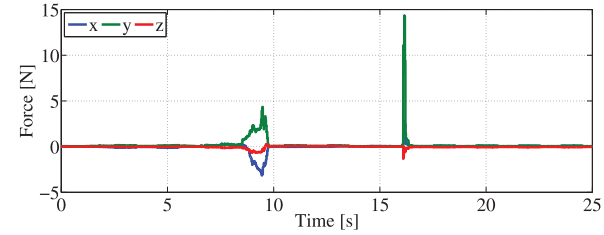

(b) Collision force components measured with the skin sensor.

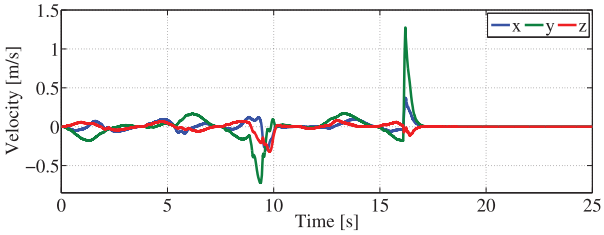

(c) Velocity of the collision point.

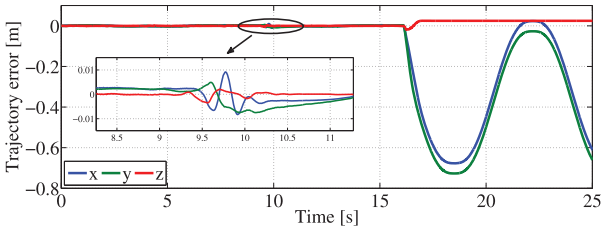

(d) Error on the end-effector trajectory.

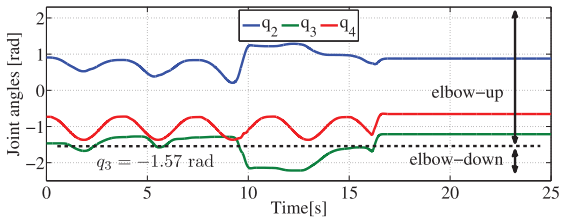

(e) Angles of joint 2, 3 and 4.

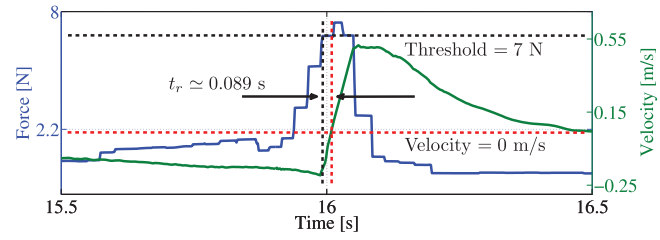

(f) Response time.

Fig. 9. First experiment.

of the whole system has been estimated. Figure 9(f) reports on the same plot a zoom view, around 16 s, of the measured net force magnitude and the velocity component along y axis, that is the main direction of motion of the collision point. The time that the velocity needs to change its sign, in which the robot reacts to the collision escaping from the contact area, is about 89 ms, meaning that only a limited amount of energy is transferred to the human during the unexpected contact. It is evident how with the good sensibility of the sensor in the estimation of the three force components and with high mechanical robustness, the skin can be used at the same time to reconfigure the robot in a fine and precise way and to escape in case of dangerous situations due to unintentional collision.

B. Second Experiment

With the second experiment, the skin sensor is used in a manual guidance task. The objective is to show how the high accuracy of the force estimation of the skin allows to use the sensor in the same way a commercial F/T sensor is usually adopted when mounted on the robot wrist, with the advantage that the skin patch can be mounted in different parts of the robot structure. In this case, the task priority is not fixed and the contact force is below the force threshold during the whole experiment. In particular, as discussed in Sec. III, the control law has been implemented in such a way that the priority of the two tasks is defined by the operator on the basis of the first point touched. The commercial sensor installed on the wrist to implement the proposed experiment is an ATI Mini45 F/T sensor. In both possible contact points, the desired position is computed by the admittance equation (3). In particular, the desired position of the end effector is computed by using the ATI sensor, while the position of the body point is computed on the basis of the data provided by the sensor skin. Two different case studies will be analyzed in order to show the robot behavior when the task priority changes, and the sensor used to manage the primary tasks switches, accordingly, from the commercial one to the skin sensor proposed in this letter.

1) Case Study I: The first case study illustrates the behavior of the robot when the operator first touches the end effector. In this case the desired position of the end effector constitutes the main task. The results are reported in Fig. 10. By observing Figs. 10(a) and 10(b) the end effector moves according to the forces exerted at the tip, measured by the commercial sensor. When the operator touches the point on the robot body (the skin sensor), the exerted forces, represented in Fig. 10(c), produce a motion in the null space of the main task. The velocities $\dot{\boldsymbol{p}}_b$, reported in Fig. 10(d), are composed by the motion allowed in the null space and the motion produced by the main task. The forces applied to the point $\boldsymbol{p}_b$ (Fig. 10(c)) and the velocities $\dot{\boldsymbol{p}}_e$ (Fig. 10(b)) clearly show that the secondary task does not affect the task with higher priority and that the motion takes place in a direction coherent with the direction of the applied force. This makes the interaction with the robot very intuitive, in contrast to a simple gravity compensation mode, that, by the way, could be applied only with a steady end effector.

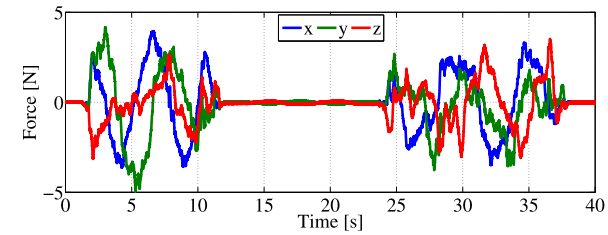

(a) Force components measured with the ATI F/T sensor.

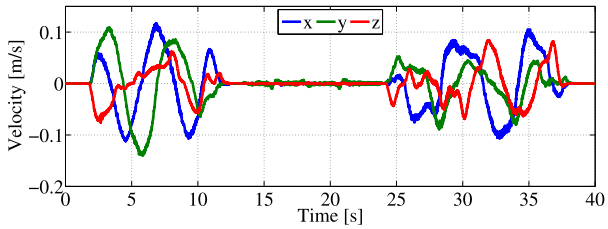

(b) Velocity in Cartesian space of the end effector.

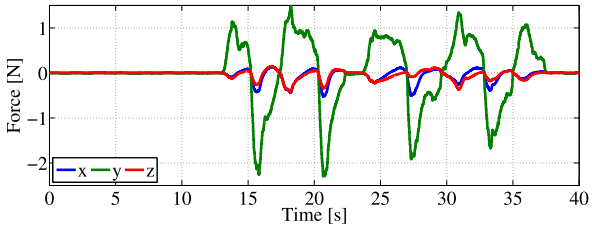

(c) Force components measured with the skin sensor.

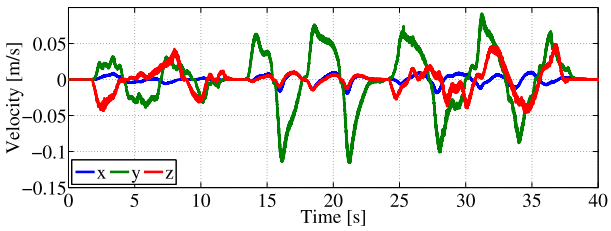

(d) Velocity in Cartesian space of the body contact point.

Fig. 10. Second experiment (case study I): all components are expressed w.r.t. the robot base frame.

2) Case Study II: Figure 11 reports a similar analysis for the second case study. The desired position of the body point is selected as the main task by first touching the point $\boldsymbol{p}_b$ on the sensor skin. Figures 11(b), 11(c) and 11(d) show that the velocities $\dot{\boldsymbol{p}}_e$ and $\dot{\boldsymbol{p}}_b$ are affected by the force $\boldsymbol{f}_b$ only. Instead, Figs. 11(a), 11(b) and 11(c) show that the end-effector motion does not generate a contribution to the velocity $\dot{\boldsymbol{p}}_b$, while it is coherent with the direction of the applied force. It is evident that in this second case the guidance of the robot, obtained by using the proposed sensor skin, is qualitatively similar to the previous case study. This experiment demonstrates that the sensibility and the accuracy of the proposed sensor, in the estimation of all contact force components, are high enough to use the sensor for intuitive guidance and programming of a robot also when the necessary measured forces are below 1N, with the advantage that the skin can be conformed to be easily mounted on different parts of the robot.

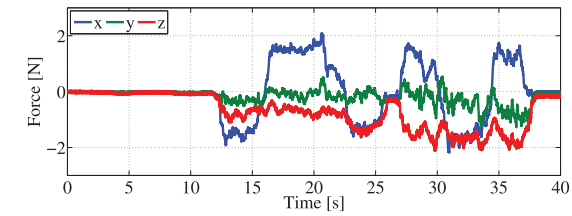

(a) Force components measured with the ATI F/T sensor.

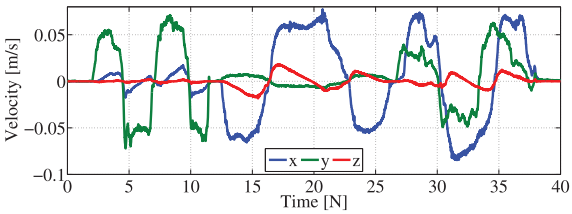

(b) Velocity in Cartesian space of the end effector.

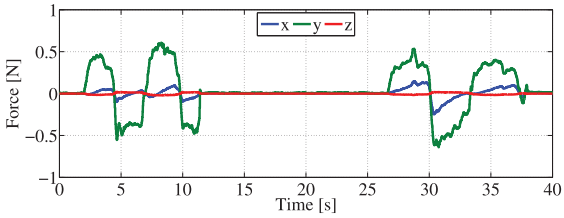

(c) Force components measured with the skin sensor.

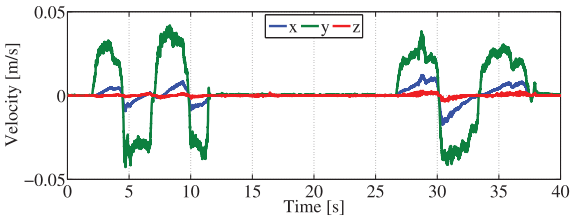

(d) Velocity in Cartesian space of the body contact point.

Fig. 11. Second experiment (case study II): all components are expressed w.r.t. the robot base frame.

V. Conclusions

In this letter a new prototype of conformable tactile skin has been presented and tested in physical HRI applications. The skin can be conformed to different parts of the external surface of a robot and allows to measure both the position of the contact point and the three components of the contact force. The use of the skin to guarantee a controlled physical HRI and a safe reaction to undesired collisions has been verified experimentally. The experiments demonstrated the sensor characteristics in real applications, by showing how the skin can be used to manage intentional and unintentional collisions at the same time. Future work will be devoted also to compare the performance obtained using the skin for direct force measurements with alternative methods, as those based on torque sensing and the so-called residual method.

References

[1] G. Cannata, M. Maggiali, G. Metta, and G. Sandini, "An embedded artificial skin for humanoid robots," in *Proc. IEEE Int. Conf. Multisensor Fusion Integr. Intell. Syst.*, 2008, pp. 434–438.

[2] N. Elkmann, M. Fritzsche, and E. Schulenbur, "Tactile sensing for safe physical human-robot interaction," in *Proc. Int. Conf. Adv. Comput. Human Interact.*, 2011, pp. 212–217.

[3] V. Duchaine, N. Lauzier, M. Baril, M. A. Lacasse, and C. Gosselin, "A flexible robot skin for safe physical human robot interaction," in *Proc. IEEE Int. Conf. Robot. Autom.*, 2009, pp. 3676–3681.

[4] X. Lamy, F. Colledani, F. Geffard, Y. Measson, and G. Morel, "Robot skin structure and performances for industrial robot comanipulation," in *Proc. IEEE Int. Conf. Adv. Intell. Mechatron.*, 2009, pp. 427–432.

[5] M. W. Strohmayr, H. Worn, and G. Hirzinger, "The DLR artificial skin step I: Uniting sensitivity and collision tolerance," in *Proc. IEEE Int. Conf. Robot. Autom.*, 2013, pp. 1004–1010.

[6] J. Ulmen and M. Cutkosky, "A robust, low-cost and low-noise artificial skin for human-friendly robots," in *Proc. IEEE Int. Conf. Robot. Autom.*, 2010, pp. 4836–4841.

[7] Y. Ohmura, Y. Kuniyoshi, and A. Nagakubo, "Conformable and scalable tactile sensor skin for curved surfaces," in *Proc. IEEE Int. Conf. Robot. Autom.*, 2006, pp. 1348–1353.

[8] T. Hoshi and H. Shinoda, "Robot skin based on touch-area-sensitive tactile element," in *Proc. IEEE Int. Conf. Robot. Autom.*, 2006, pp. 3463–3468.

[9] M. Fumagalli, M. Randazzo, F. Nori, L. Natale, G. Metta, and G. Sandini, "Exploiting proximal F/T measurements for the iCub torque control," in *Proc. IEEE/RSJ Int. Conf. Intell. Robots Syst. (IROS)*, 2010, pp. 1870–1876.

[10] A. Del Prete *et al.*, "Skin spatial calibration using force/torque measurements," in *Proc. IEEE/RSJ Int. Conf. Intell. Robots Syst. (IROS)*, 2011, pp. 3694–3700.

[11] M. Fumagalli *et al.*, "Force feedback exploiting tactile and proximal force/torque sensing," in *Autonomous Robots*. New York, NY, USA: Springer, 2012, vol. 33, pp. 381–398.

[12] R. S. Dahiya, P. Mittendorfer, M. Valle, G. Cheng, and V. J. Lumelsky, "Directions toward effective utilization of tactile skin: A review," *IEEE Sens. J.*, vol. 13, no. 11, pp. 4121–4138, Nov. 2013.

[13] F. Flacco and A. De Luca, "Integrated control for pHRI: Collision avoidance, detection, reaction and collaboration," in *Proc. 4th IEEE RAS/EMBS Int. Conf. Biomed. Robot. Biomechatron.*, 2012, pp. 288–295.

[14] E. Magrini, F. Flacco, and A. De Luca, "Estimation of contact forces using a virtual force sensor," in *Proc. IEEE/RSJ Int. Conf. Intell. Robots Syst.*, 2014, pp. 2126–2133.

[15] H. Sadeghian, L. Villani, M. Keshmiri, and B. Siciliano, "Task-space control of robot manipulators with null-space compliance," *IEEE Trans. Robot.*, vol. 30, no. 2, pp. 493–506, Apr. 2014.

[16] F. Ficuciello, A. Romano, L. Villani, and B. Siciliano, "Cartesian impedance control of redundant manipulators for human-robot co-manipulation," in *Proc. IEEE/RSJ Int. Conf. Intell. Robots Syst.*, 2014, pp. 2120–2125.

[17] F. Ficuciello, L. Villani, and B. Siciliano, "Variable impedance control of redundant manipulators for intuitive human-robot physical interaction," *IEEE Trans. Robot.*, vol. 31, no. 4, pp. 850–863, Aug. 2015.

[18] A. Cirillo, P. Cirillo, G. De Maria, C. Natale, and S. Pirozzi, "An artificial skin based on optoelectronic technology," *Sens. Actuat. A Phys.*, vol. 212, pp. 110–122, 2014.

[19] H. Sadeghian, L. Villani, M. Keshmiri, and B. Siciliano, "Dynamic multi-priority control in redundant robotic systems," *Robotica*, vol. 31, pp. 1155–1167, 2013.

[20] G. De Maria, C. Natale, and S. Pirozzi, "Force/tactile sensor for robotic applications," *Sens. Actuat. A Phys.*, vol. 175, pp. 60–72, 2012.

[21] A. Cirillo, P. Cirillo, G. De Maria, C. Natale, S. Pirozzi, "A FE analysis of a silicone deformable interface for distributed force sensors," in *Proc. 7th Int. Conf. Times Polimers Compos.*, 2014, pp. 485–488.

[22] A. A. Maciejewski and C. A. Klein, "Numerical filtering for the operation of robotic manipulators through kinematically singular configurations," *J. Robot. Syst.*, vol. 5, pp. 527–552, 1988.